

Spatial and temporal structures of turbulent bubble-driven flows in a rectangular water tank[†]

Seung Jae Yi, Sang Moon Kim, Hyun Dong Kim, Jong Wook Kim and Kyung Chun Kim*

*Micro-Bio Fluidics Laboratory, School of Mechanical Engineering, Pusan National University,
San 30, Jangjeon-dong Geumjeong-gu Busan 609-735, Korea*

(Manuscript Received January 19, 2010; Revised April 20, 2010; Accepted June 2, 2010)

Abstract

The spatial and temporal structures of turbulent water flows driven by air bubbles in a rectangular water tank were investigated. The time-resolved particle image velocimetry (PIV) technique was adopted for quantitative visualization. Flow rates of compressed air were changed from 2 to 4 ℓ/min at 0.5 MPa, and the corresponding range of bubble-based Reynolds number ranged from 6,740 to 13,220. The dynamics of flow structures was further investigated by the time-resolved proper orthogonal decomposition (POD) analysis technique. When the flow rate was increased, the main vortex core moved to the side and bottom wall. Locations of peak turbulent kinetic energy regions depended on the bubble Reynolds number. Both spatial and temporal modes were quite different with respect to the flow rates. The first temporal mode was harmonized with the second temporal mode, with small oscillations in the case of the lowest Reynolds number. However, temporal modes oscillate with higher frequencies when the Reynolds number increases. Based on the result of the FFT analysis of each temporal mode, we conjectured that low-frequency oscillation was attributed to the recirculating flow, whereas a higher dominant frequency was related to the vibration of the free surface that interacts with the rising bubbles.

Keywords: Bubble-driven flow; Time-resolved PIV; Proper orthogonal decomposition; Turbulence structure

1. Introduction

Bubble-driven flow is significant to various engineering systems, such as nuclear waste treatment, bio-chemical reactors, and steel-making plants. In chemical engineering and industrial fields, problems with mixing, such as powder dispersion, solid blending, and gas dispersion into liquid, have been important issues because product quality and productivity highly depend on it [1-3].

Despite the extensive applications of this basic flow phenomenon, the design of these engineering systems has been mainly based on trial and empirical methods. Thus, a detailed examination of mass, momentum, and energy transfer is essential to improve and optimize the design of these industrial processes. However, the complexity of the fluid's turbulent dynamics, three-dimensional two-phase flow, and the coalescence and break-up of bubbles, has prevented researchers from devising comprehensive modeling procedures and establishing design rules.

There are two main interests in turbulent bubble flow stud-

ies: turbulence modification by bubbles and turbulent mixing due to bubble-driven liquid flows. Previous studies on turbulence modification have shown that dispersed bubbles can either augment or attenuate the turbulent kinetic energy of the liquid phase [4, 5]. Fujiwara et al. [6] conducted an experimental investigation of a vertical pipe flow injected with dispersed bubbles using particle image velocimetry (PIV)/laser-induced fluorescence (LIF) and projecting shadow image technique. They found that a high concentration of bubbles in the vicinity of the wall induces a reduction of the fluctuation velocity intensity of the liquid. However, the external force that is affected by the bubbles is expected to contribute to the production of turbulence energy.

Durst et al. [7, 8] experimented on bubble-driven laminar flows by investigating liquid circulation and motion of bubbles using a laser-Doppler system. The liquid-phase circulation pattern was found to be insensitive to the actual shape of the void fraction profiles. Johansen et al. [9] studied fluid dynamics in bubble-stirred ladles by employing a laser-Doppler system to measure the axial and radial mean velocities and fluctuating velocities of the liquid phase. Air was supplied through a porous plug placed at the bottom wall of a cylindrical perspex model of a ladle. Recently, Montante et al. [10] measured turbulent gas-liquid flow and bubble size distribution in aerated stirred tanks using a two-phase PIV and a digi-

[†]This paper was recommended for publication in revised form by Associate Editor Haecheon Choi

*Corresponding author. Tel.: +82 51 510 2324, Fax: +82 51 515 7866

E-mail address: kckim@pusan.ac.kr

© KSME & Springer 2010

tal image processing method based on a threshold criterion. However, pure bubble-induced flow was not used; rather, a Rushton turbine was included in the mixing tank.

Druault et al. [11] developed a new proper orthogonal decomposition (POD) application to recover information between two consecutive PIV time measurements based on time-resolved PIV data of in-cylinder engine flows. By performing a POD over the full PIV velocity field snapshots, resulting POD coefficients were time-interpolated in order to have a continuous space–time description of the turbulent flow field. The study concluded that such interpolation procedure could be applied to any time-resolved PIV data for turbulent flow fields.

Most bubble-induced flows were investigated in an axisymmetric tank. In this study, a rectangular tank was chosen to acquire clearer and undistorted images. Such data can help in understanding dynamic flow structures based on the time-resolved PIV technique, which requires accurate quantitative visualization. The aim of this study is to understand mixing characteristics in the vitrification process of radioactive wastes using an induction cold crucible melter (CCM) to find the optimal operating conditions and design guidelines.

Because mixing characteristics in bubble-driven turbulent liquid flow are strongly governed by large-scale motions in the flow field, an analysis of large-scale dynamics is necessary to understand the mixing mechanism. We measured the entire flow field and analyzed large-scale dynamic structures and turbulent characteristics in bubble-driven water flow in a rectangular tank using time-resolved PIV and POD techniques for the bubbling mixer.

2. Experimental set-up

Fig. 1 shows a schematic diagram of the experimental set-up. A cube is made of transparent acrylic panels with a length of 0.3 m in each dimension. Tap water was used as the working fluid, and compressed air formed the bubble stream. The height of the free surface is 150 mm from the bottom wall. An air injection nozzle with a nozzle diameter (D_N) of 5 mm was placed at the center of the bottom wall. The exit of the nozzle is located 42 mm above the bottom wall. Compressed air was supplied to the nozzle through a regulator valve, and a flow meter was used to precisely control the flow rate of air. The flow rate of compressed air varied from 2 to 4 l/min at an air pressure of 0.5 MPa.

To reduce diffused reflections originating from the bubbles and the nozzle, fluorescent polymer particles (Dantec dynamics) were used. The maximum excitation wavelength of the particles is 550 nm, and the maximum emission wavelength is 590 nm. A laser beam 5 mm in diameter originating from a 532-nm diode CW laser passed through a spherical lens and a cylindrical lens and turned into a 2 mm thick sheet beam. The sheet beam irradiated the object plane through the transparent side wall. A 10-bit high-speed CMOS camera (1,280 × 1,024 pixels, pco. 1,200 hs, PCO) was used with a 545-nm long-pass

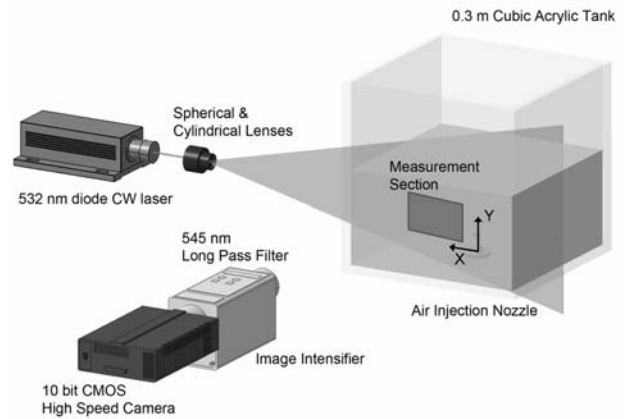


Fig. 1. Schematic diagram of the experimental set-up.

optical filter mounted on its lens to eliminate diffused reflections. An image intensifier (UVI 507, Invisible Vision Ltd) was used to acquire enhanced clean particle images. The size of the field-of-view is 120 mm × 100 mm. It was chosen to acquire the whole field of bubble-driven water flow just below the oscillating free surface and beside the bubble stream to avoid optical disturbances. A typical two-dimensional time-resolved PIV system was adopted. For each case, 1,000 images were acquired, with time interval of 12.5 ms (80 frames/s) between images, and the images were interrogated using a two-frame cross-correlation technique. Interrogation windows were set at 48 × 48 pixels; the FFT window size was set at 64 × 64 pixels; and a 50% window overlap was adopted. False vectors in the raw vector fields were eliminated using the magnitude difference technique with 80% threshold. They were then interpolated with a 3 × 3 Gaussian convolution.

3. Proper orthogonal decomposition

Dynamic information of the flow field can be explained effectively by the POD, from which the relative energy distribution was acquired. By using the POD technique as proposed by Lumley, the flow field can be decomposed into optimal orthogonal spatial modes and optimal orthogonal temporal modes [12].

$$\mathbf{u}(\mathbf{x}, t) = \sum_n a^{(n)}(t) \boldsymbol{\phi}^{(n)}(\mathbf{x}) \quad (1)$$

Optimality means that POD minimizes the mean square error of any partial sum of expansion and, conversely, expansion in terms of these bases obtained by POD converges faster than the expansion in terms of any other basis, such as the Fourier decomposition. Spatial modes can be obtained by solving the following integral equation:

$$\int R(\mathbf{x}, \mathbf{x}') \boldsymbol{\phi}^{(n)}(\mathbf{x}') d\mathbf{x}' = \lambda^{(n)} \boldsymbol{\phi}^{(n)}(\mathbf{x}) \quad (2)$$

where λ is the eigenvalue and the ensemble-averaged two-point correlation function. The orthogonality of spatial and

Table 1. Flow conditions and dimensionless values.

| Case | D_N (mm) | D_B (mm) | V_B (m/s) | Bubblefrequency (Hz) | Re | Eo |
|------|---------------|---------------|----------------|-------------------------|--------|----|
| I | 5 | 21.8 | 0.31 | 13.5 | 6,744 | 64 |
| II | 5 | 24.0 | 0.39 | 14.0 | 9,341 | 77 |
| III | 5 | 25.0 | 0.53 | 15.0 | 13,223 | 84 |

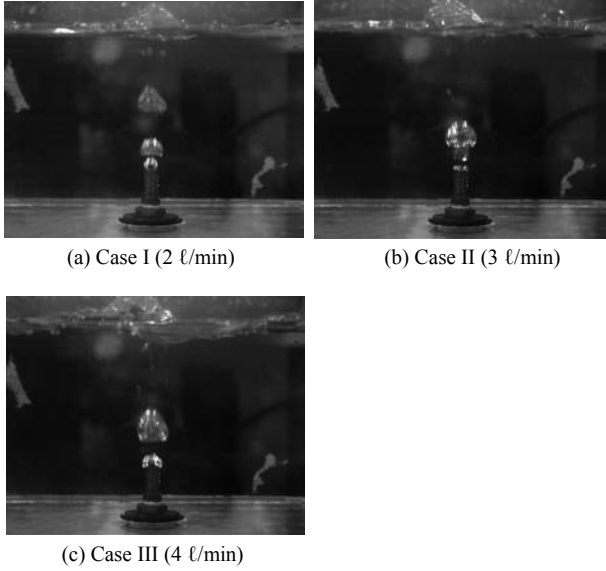


Fig. 2. Flow visualization image of bubble stream and free surface fluctuation in the tank. (a) Case I (2 l/min), (b) Case II (3 l/min) and (c) Case III (4 l/min).

temporal bases is represented as follows:

$$\left(\phi^{(n)}(\mathbf{x}), \phi^{(m)}(\mathbf{x}')\right) = \delta_{nm}, \quad \langle a^{(n)}(t), a^{(m)}(t) \rangle = \lambda^{(n)} \delta_{nm} \quad (3)$$

Because the traditional direct method requires many calculations, thus taking up much time, Sirovich [13] suggested the snapshot method, which can save calculation time. In this research, we executed a POD analysis using the snapshot method and the instantaneous fluctuating velocity field in order to find the dynamic structures:

$$\mathbf{u}(\mathbf{x}, t) = \bar{\mathbf{u}}(\mathbf{x}) + \mathbf{u}'(\mathbf{x}, t) = \bar{\mathbf{u}}(\mathbf{x}) + \sum_{m=1}^M a^{(m)}(t) \phi^{(m)}(\mathbf{x}) \quad (4)$$

From the calculated eigenmodes, spatial and temporal modes were derived. Temporal modes represent the time variations of energy in the corresponding spatial modes. Thus, movement of the dominant flow structures relative to frequency can be obtained mathematically.

From these data, we extracted the turbulent kinetic energy contribution and compared it with a large-scale structure using the sum of the first few modes.

4. Results and discussion

Fig. 2 shows a flow visualization image of the bubble

stream and free surface fluctuation in the tank. The detached bubble size at the nozzle exit is about two times larger than the nozzle diameter. However, the combined bubbles and final size of the rising bubbles near the free surface become 4–5 times larger than the nozzle diameter. Increasing the flow rates causes the mean diameter and mean velocity of the bubbles to increase. The frequency at which the bubbles are detached from the nozzle slightly increases as well. The velocities of the bubble rise are not exactly proportional to the air flow rates.

The shape of the developed air bubble looks like a cone (Fig. 2). The terminal velocity of the bubble can be calculated using the following equation:

$$V = \left[\frac{4}{3} \frac{\rho_{\text{water}} - \rho_{\text{air}}}{\rho_{\text{water}}} \frac{g D_B}{C_D} \right]^{1/2} \quad (5)$$

Assuming that the drag coefficient C_D is 1.15 (cone with $\theta = 90^\circ$) for case III [14], the obtained terminal velocity is 0.59 m/s. Compared to the measured bubble rise velocity of 0.53 m/s, the calculated value of the terminal velocity shows good agreement with the measurement.

Reynolds and Eötvös numbers were calculated according to the following equations:

$$\text{Re} = \frac{\text{inertial force}}{\text{viscous force}} = \frac{\rho_w V_B \cdot D_B}{\mu_w} \quad (6)$$

$$\text{Eo} = \frac{\text{lift force}}{\text{surface tension force}} = \frac{g \Delta \rho D_B^2}{\sigma} \quad (7)$$

where ρ_w is the density of the working fluid, V_B is the mean rise velocity of the bubbles, D_B is the mean diameter of the bubbles calculated from the images, μ_w is the absolute viscosity of the working fluid, g is the acceleration due to gravity, $\Delta \rho$ is the difference in density between the two phases, and σ is the surface tension of the interfacial layer. The obtained flow parameters are listed in Table 1.

When the Eo and Re values of the three cases are plotted on the shape regime graph [15], all are located in the regime of the “spherical cap” shape, which is similar to the shape of the bubbles (cone shape, Fig. 2). Because air bubbles disappear at the free surface, there is no gas phase in the measurement volume. The buoyancy-driven kinetic energy of the bubble-generated recirculation flow in the liquid, as well as the waves at the free surface.

Fig. 3 shows the time-averaged velocity fields induced by bubbles for each case. A total of 999 instantaneous velocity fields were ensemble-averaged to obtain the mean velocity field. There is an upward flow that was driven by the bubble stream on the right half of the vector plots, and a counter-clockwise large vortical structure is located at the upper left side. There is also inward flow at the right-bottom side of the view, which is induced by rising air bubbles. When the time-averaged velocity fields for each case were compared, we observed a movement of the center of the vortical structure.

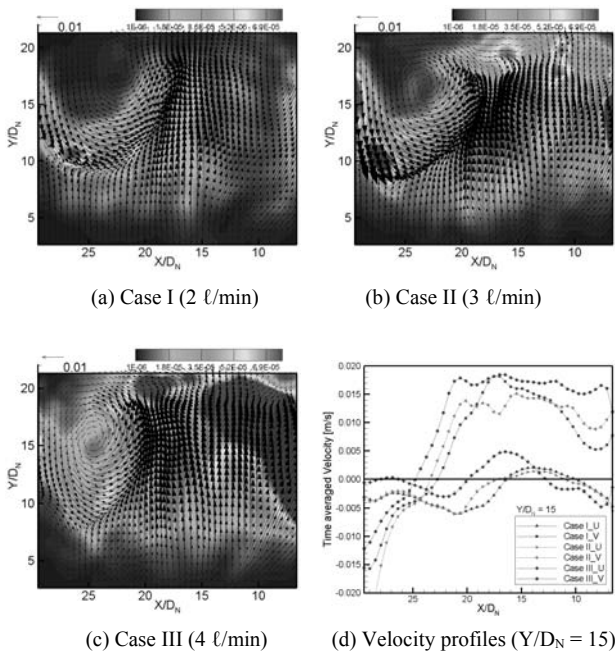


Fig. 3. Mean velocity vector fields with turbulent kinetic energy contour for each case: (a) case I (2 l/min), (b) case II (3 l/min), (c) case III (4 l/min), and (d) velocity profiles at $Y/D_N = 15$.

As the flow rate of compressed air increases, the center of the vortex moves outward and downward. In case I, the core location of the structure is at $X/D_N = 22.5$ and $Y/D_N = 18.2$, whereas in case III, the core location of the structure moves to $X/D_N = 24.5$ and $Y/D_N = 15.5$. Core location can be affected by the chamber size, depth of liquid, size of the nozzle, and flow rates of gas, among others. However, in the present experiment, all parameters were fixed, except for the flow rates. We believe that the increased flow of compressed air transfers more upward kinetic energy to the working fluid and that the faster-moving working fluid gains more inertial force, which in turn pushes the vortical structure outward and makes it narrower. Therefore, the center of the structure moves outward. Due to the existence of a free surface and the side wall of the tank, the center of the structure moves downward.

The mean velocity profiles along $Y/D_N = 15$ are shown in Fig. 3(d). The horizontal line at $Y/D_N = 15$ passes the vortex cores. The horizontal velocity component U depicts similar behavior for all three cases in terms of direction and magnitude. However, the vertical velocity component V varies with the air flow rate. As the flow rate increases, the vertical velocity induced by the gas bubbles becomes stronger and wider [Fig. 3(d)]. Note that the magnitude of vertical velocity is quite low (0.015–0.020 m/s) compared with the bubble rise velocity (0.31–0.53 m/s). The uniform vertical flow area was observed between the recirculating region and the bubble rise region. Bubble velocity increases with increasing gas flow rate. However, the induced vertical flow due to viscosity is not strong in the regime with a high Reynolds number.

The contour in Fig. 3 illustrates the turbulent kinetic energy

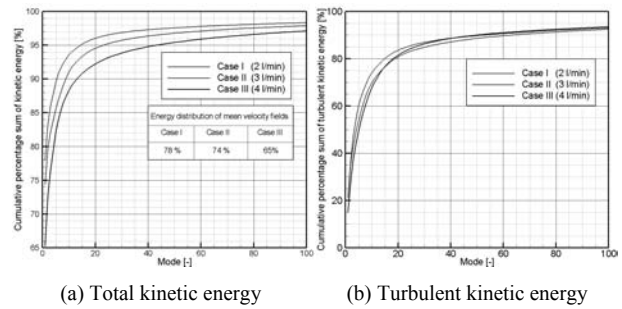


Fig. 4. Cumulative energy distributions of each case: (a) cumulative percentage sum of the total kinetic energy and (b) cumulative percentage sum of the turbulent kinetic energy.

distribution of each case. In case I, the greatest turbulent kinetic energy is located at the recirculating zone, whereas in case III, it is located at the right side near the bubble rising region. In case II, peak values of the turbulent kinetic energy are found in the recirculating region near the free surface and in the vicinity of the bubble rising region. We conclude that the dominant mechanism of turbulence generation strongly depends on the Reynolds number of the bubble-driven water flow. In the visualization study, bubbles move with more vigorous agitation, and the fluctuation of the free surface becomes stronger as the gas flow rate increases.

In our POD analysis, the eigenvalue represents the turbulent kinetic energy of each mode. Fig. 4 demonstrates the turbulent kinetic energy distribution and the corresponding cumulative energy sum with respect to the mode number for each case. The time-mean flow field has 78% of the total kinetic energy at case I. This means that the dominant dynamic structure in the set of instantaneous velocity fields is the time-averaged recirculating motion. Most turbulent kinetic energy is concentrated on the first few percent of the total number of modes. For example, the first 20 modes have 83.6% of the total turbulent kinetic energy (96.1% of the total kinetic energy) in case I. The time-averaged velocity fields of cases II and III have 74% and 65% of the total kinetic energy, respectively. With increasing Reynolds numbers, the energy-cascading process begins at higher modes, and the energy spectrum of the turbulent transport becomes wider. This behavior is shown in Fig. 4(a): the cumulative kinetic energy increases slowly along with increasing air flow rate. The cumulative percentage sum of the turbulent kinetic energy also shows similar behaviors, [Fig. 4(b)].

Figs. 5–7 show the four spatial and temporal modes in order. They represent the dynamics of large-scale motions in turbulent mixing flow for three different flow rates. Fig. 5 demonstrates the initial eigenmodes at the flow rate of 2 l/min. The first spatial mode contains the largest turbulent kinetic energy. From Fig. 5(a), one can recognize the upward rising flow because of a vortex rotating counter-clockwise at the right side and another vortex rotating clockwise near the upper side of the wall. Two vortices make a counter-rotating vortex pair. Several small-scale vortices are observed in the second spatial

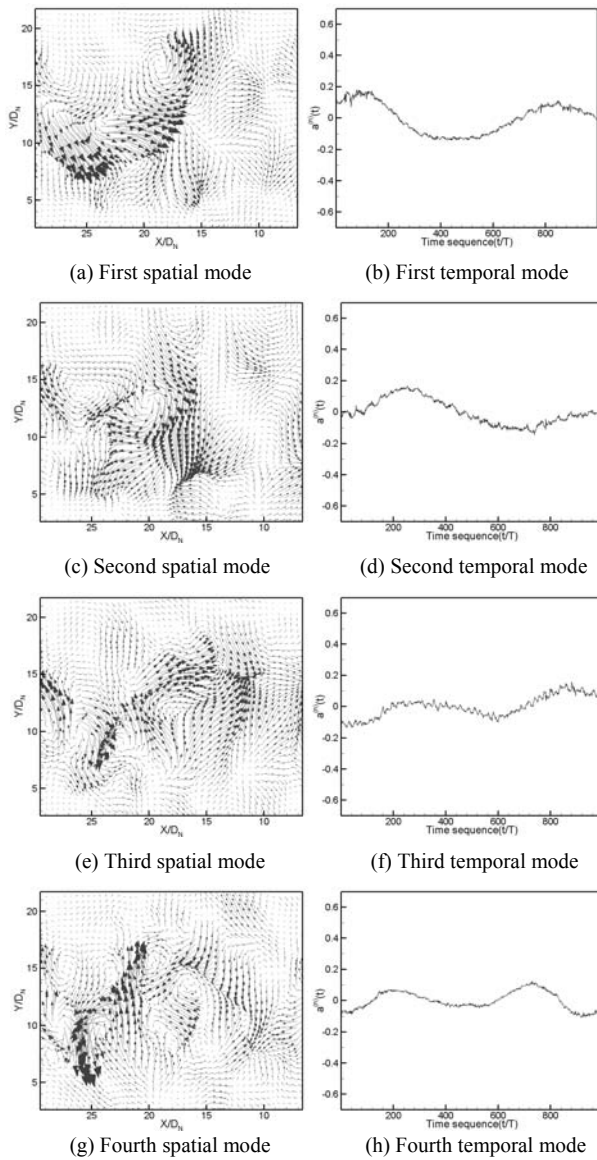


Fig. 5. First four eigenmodes of case I: (a) first spatial mode, (b) first temporal mode, (c) second spatial mode, (d) second temporal mode, (e) third spatial mode, (f) third temporal mode, (g) fourth spatial mode, and (h) fourth temporal mode.

mode [Fig. 5(c)]. These structures are randomly distributed in the flow field, such that the averaged velocity field has a single large-scale vortex in the measurement plane. Figs. 5(e) and 5(g) show the third and fourth eigenmodes, which reveal that the large-scale structure becomes smaller and smaller throughout the turbulent energy-cascading process.

The higher modes that appear in Figs. 5(e) and 5(g) are not the dominant structures in the overall flow field, compared with the first and second modes. However, these motions certainly contribute to turbulent mixing behavior. The temporal mode represents the time variation of energy contained in the corresponding spatial mode. We conjectured that the temporal mode illustrates the associated time scales with the corresponding spatial mode. The first temporal mode of case I

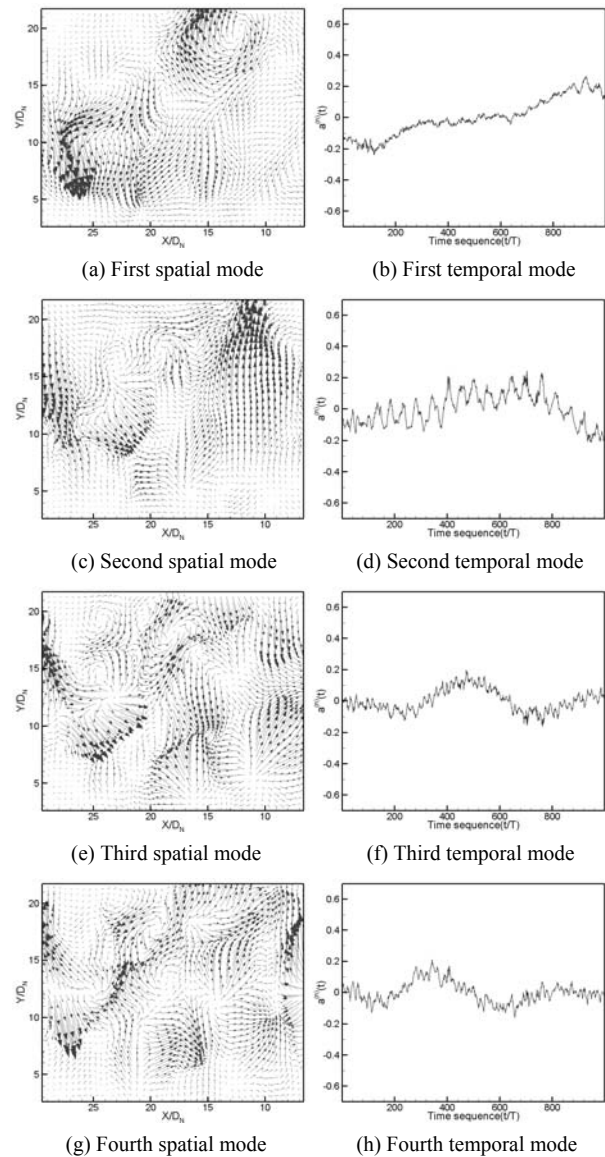


Fig. 6. First four eigenmodes of case II: (a) first spatial mode, (b) first temporal mode, (c) second spatial mode, (d) second temporal mode, (e) third spatial mode, (f) third temporal mode, (g) fourth spatial mode, and (h) fourth temporal mode.

shows very slow sinusoidal oscillation [Fig. 5(b)]. The second temporal mode has the same frequency as that of the oscillation, but there is a phase lag between the first and second temporal modes [Fig. 5(d)]. The third and fourth temporal modes that are shown in Figs. 5(f) and 5(h) have the same frequency and phase, but their frequency is twice that of the first and second modes.

Fig. 6 shows large-scale motions in the case with a flow rate of 3 ℓ/min . The salient feature of the first spatial mode [Fig. 6(a)] is that the high momentum zones coincide with the high turbulent kinetic energy regions [Fig. 3(b)]. The second spatial mode depicts high-speed upward vertical motion to the free surface and downward vertical flow at the side wall. As the flow rate of air increases, the velocity of the bubbles also

increases, causing the associated vibrating motion to generate more turbulence. The increased kinetic energy of the bubbles creates free surface vibration, followed by increased rising velocity near the free surface, and randomly distributed smaller vortices in higher eigenmodes [Figs. 6(e) and 6(g)]. There are several counter-rotating vortices inside the mean recirculating zone. Many saddle points are found in the third and fourth spatial modes, indicating that three-dimensional motion of large-scale eddies increases compared to that in case I.

Temporal modes in case II are similar to those in case I. However, high-frequency oscillation was added to the low-frequency motion. High-frequency oscillation can be attributed to the unsteady bubbling motion. Fig. 7 shows the four eigenmodes present when the air flow rate is 4 l/min. Both the spatial and temporal modes are quite different from those shown in Figs. 5 and 6. The first spatial mode [Fig. 7(a)] represents the high-momentum upward vertical flow that is due to the rising bubbles near the free surface, and the location coincides with the high turbulent kinetic energy region shown in Fig. 3(c). A weak vertical flow pattern is also observed in the mean recirculating zone. The second spatial mode contains three different dynamics [Fig. 7(c)]. Upward vertical flow occurs near the free surface, two counter-rotating vortices appear in the region of the mean recirculation, and a push-flow pattern is observed from the bubble rising zone. As expected from the mean turbulent kinetic energy distribution of case III [Fig. 3(c)], turbulence production from rising bubbles seems significant compared to that of cases II and III. The third spatial mode shows only a push-flow pattern from the rising bubbles [Fig. 7(e)]. An interesting feature of the fourth spatial eigenmode is a suction flow mode due to the rising bubbles [Fig. 7(g)]. The low-pressure region in the wake behind the moving bubbles is considered to entrain the nearby liquid.

The first temporal mode shows a beating nature combining a low-frequency and a high-frequency harmonic oscillation [Fig. 7(b)]. The second temporal mode [Fig. 7(d)] looks similar with the first temporal mode, but it contains much higher frequencies. Fig. 7(f) shows that the third temporal mode oscillates with a higher frequency compared with lower modes. The fourth temporal mode [Fig. 7(h)] is the same as the third mode, indicating that both the third and fourth modes are associated with bubble dynamics in case III. Unlike cases I and II, small-scale vortical motions do not appear in the first four spatial modes because energy-containing eddies are dominated by higher bubble rising velocities and free surface flows.

Figs. 8–10 show the FFT analysis results of each temporal mode. There are many different time scales in the bubble-driven flow, such as eddy turnover time scale, bubble-generating time scale, and surface-wave-induced time scale. The first temporal mode of case I shows very slow sinusoidal oscillation with a frequency of 0.08 Hz [Fig. 8(a)]. This kind of low-frequency unsteadiness has been observed for an impinging jet with a low Reynolds number in a confined wall

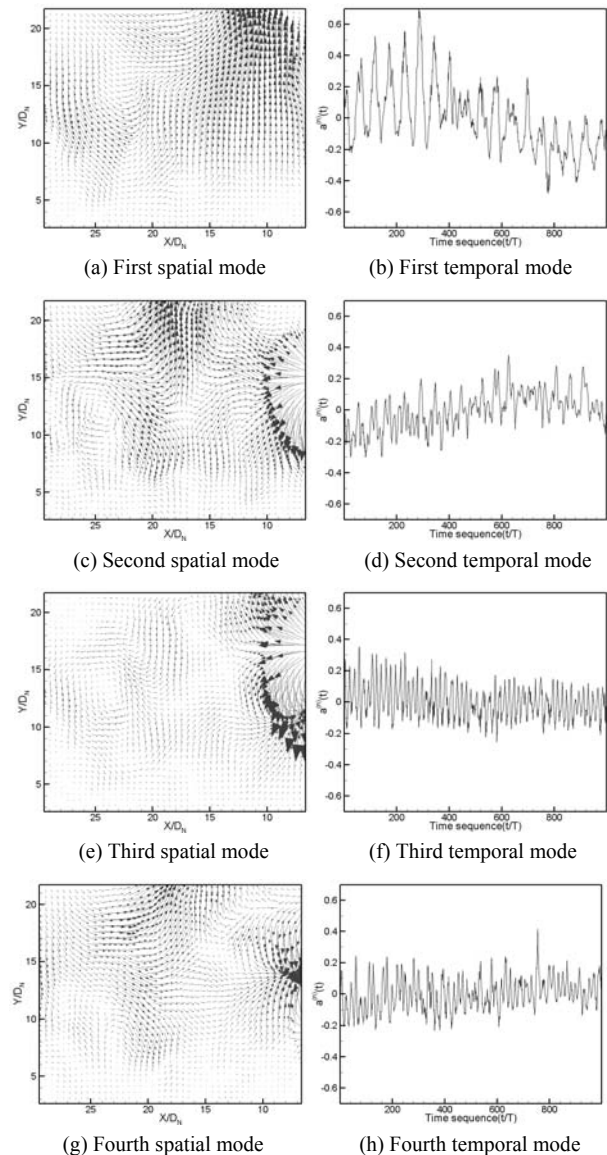


Fig. 7. First four eigenmodes of case III: (a) first spatial mode, (b) first temporal mode, (c) second spatial mode, (d) second temporal mode, (e) third spatial mode, (f) third temporal mode, (g) fourth spatial mode, and (h) fourth temporal mode.

(Kim et al. [16]). Since the bubble flow rising to the free surface is similar to the impinging jet to a normal wall, low-frequency oscillation can be explained as a kind of sloshing motion of the free surface or the bubble jet. The second temporal mode has the same peak at a frequency of 0.08 Hz. The third and fourth temporal modes [Figs. 8(c) and 8(d)] have a frequency of 0.16 Hz, which is twice that of the first and second modes.

The FFT results of the first and second temporal modes of case II have peaks at 0.08 Hz, which is the same as that of case I [Figs. 9(a) and 9(b)]. However, there is another peak at a frequency of 1.523 Hz in the second temporal mode.

We conjectured that the higher dominant frequency oscillation might be related to vibration of the free surface, which

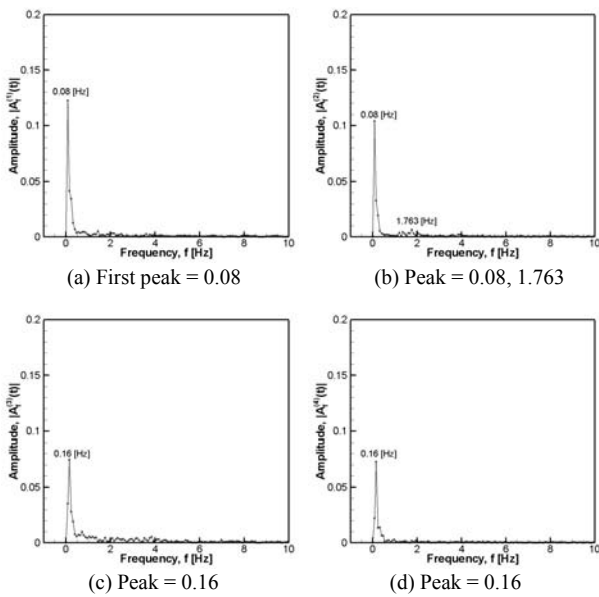


Fig. 8. FFT results of case I (2 l/min): (a) first temporal mode, (b) second temporal mode, (c) third temporal mode, and (d) fourth temporal mode.

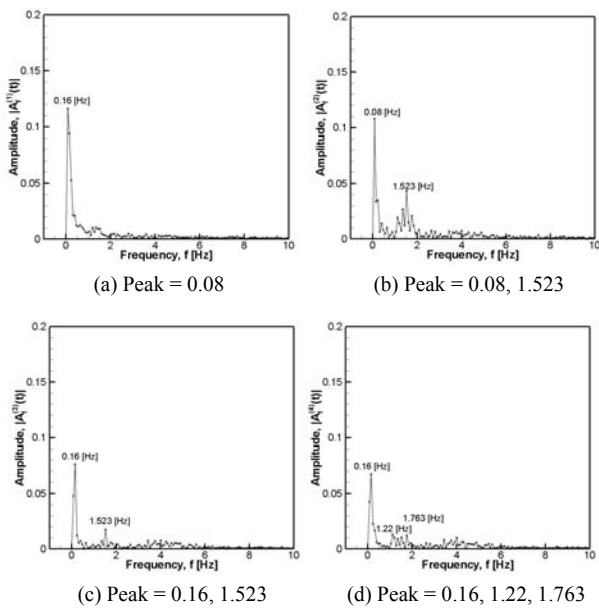


Fig. 9. FFT results of case II (3 l/min): (a) first temporal mode, (b) second temporal mode, (c) third temporal mode, and (d) fourth temporal mode.

interacts with the rising bubbles. This frequency is quite low compared to the bubble-generation frequency of 14.0 Hz at the nozzle exit. Therefore, this frequency may be related to the free surface wave. Unfortunately, we did not measure the frequency of the free surface oscillation. The peaks of the FFT results of the third and fourth temporal modes [Figs. 9(c) and 9(d)] occurred at a frequency of 0.16 Hz, which is twice the peak frequency of the first and second temporal modes.

Fig. 10 demonstrates the FFT result of the temporal modes

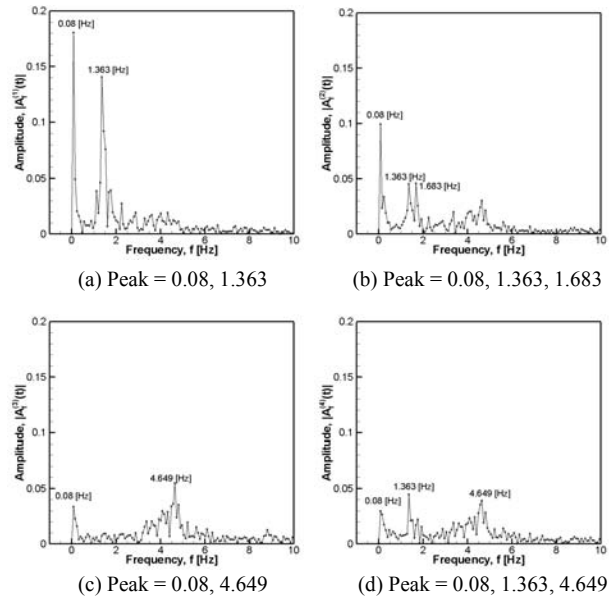


Fig. 10. FFT results of case III (4 l/min): (a) first temporal mode, (b) second temporal mode, (c) third temporal mode, and (d) fourth temporal mode.

in case III. The first temporal mode [Fig. 10(a)] oscillates with two distinct frequencies: 0.08 Hz and 1.363 Hz. The lower frequency may be attributed to the recirculating flow near the side wall, and its value is the same as that of the first mode in case I. The higher frequency of 1.363 Hz may be associated with the vibration of the free surface. The spectrum of the second temporal mode shows a similar nature as that of the first mode, but the magnitudes of the peaks are reduced [Fig. 10(b)]. The third and fourth temporal modes show a rather broad spectrum compared with that of the first and second modes. The maximum peak appeared at a frequency of 4.649 Hz [Figs. 10(c) and (d)]. Although this frequency is lower than the bubble-generating frequency at the nozzle exit (15 Hz), it may be related to the oscillation of rising bubbles because the corresponding spatial modes demonstrate bubble-related motions.

5. Conclusion

In order to investigate the spatial and temporal structures of bubble-driven turbulent water flow with three different air flow rates, an experimental study was conducted using the time-resolved PIV and POD techniques. Even though the time-averaged mean flow fields show similar flow patterns for all cases, the dynamic characteristics of large-scale turbulent motions are significantly different with respect to the Reynolds number of the bubble.

In case I, most turbulent kinetic energy and large-scale motions are concentrated in the mean recirculating zone. The first two temporal modes are highly correlated with each other, resulting in harmonic oscillation. As the Reynolds number of the bubble increases, dominant turbulent motions are generated by the bubbles. The first four spatial modes obtained in

case III vividly demonstrate outward and inward flow dynamics due to the unsteady bubble motions. From the result of the FFT analysis of each temporal mode, it is conjectured that the low frequency may be attributed to the recirculating flow near the side wall, and the higher dominant frequency oscillation may be related to the vibration of the free surface, which interacts with the rising bubbles.

Acknowledgment

This research is supported by the Korea Science and Engineering Foundation (KOSEF) grant funded by the Korea government (MEST) (No. 2009-0080535). The first and third authors are supported by the second phase of the Brain Korea 21 Program in 2009.

Nomenclature

| | |
|----------------|--|
| ρ_{water} | : Density of water |
| ρ_{air} | : Density of air |
| g | : Acceleration of gravity |
| D_B | : Mean diameter of bubbles |
| D_N | : Diameter of nozzle |
| V_B | : Mean rise velocity of the bubble |
| C_D | : Drag coefficient |
| μ_w | : Absolute viscosity of water |
| σ | : Surface tension of the interface layer |

References

- [1] W. Luewisutthichat, A. Tsutsumi and K. Yoshida, Chaotic Hydrodynamics of Continuous Single-Bubble Flow Systems, *Chemical Engineering Science*, 52 (1997) 3685-3691.
- [2] P. Tirto, T. Koichi and T. Hideki, Effect of Operating Conditions on Two-Phase Bubble Formation Behavior at Single Nozzle Submerged in Water, *Journal of Chemical Engineering*, 34 (2001) 114-120.
- [3] X. Tu and C. Trägårdh, Methodology development for the analysis of velocity particle image velocimetry images of turbulent, bubbly gas-liquid flows, *Measurement Science & Technology*, 13 (2002) 1079-1086.
- [4] T. G. Theofanous and J. Sullivan, Turbulence in Two-phase Dispersed Flows, *Journal of Fluid Mechanics*, 116 (1982) 343-362.
- [5] S. K. Wang, S. J. Lee, O. C. Jones Jr. and R. T. Lahey Jr., Turbulence Structure and Phase Distribution Measurements in Bubbly Two-phase Flows, *International Journal of Multiphase Flow*, 13 (1987) 327-343.
- [6] A. Fujiwara, D. Minato and K. Hishida, Effect of Bubble Diameter on Modification of Turbulence in an Upward Pipe Flow, *International Journal of Heat and Fluid Flow*, 25, (2004) 481-488.
- [7] F. Durst, A.M.K.P. Taylor and J. H. Whitelaw, Experimental and Numerical Investigation of Bubble-driven Laminar Flow in an Axisymmetric Vessel", *International Journal of Multiphase Flow*, 10, (1984) 557-569.
- [8] F. Durst, B. Schönung, K. Selanger and M. Winter, Bubble-driven liquid flows, *Journal of Fluid Mechanics*, 170 (1986) 53-82.
- [9] S. T. Johansen, D.G.C. Robertson, K. Woje and T.A. Engh, Fluid Dynamics in Bubble Stirred Ladles: Part I. Experiments, *Metallurgical Transactions*, 19B (1988) 745-754.
- [10] G. Montante, D. Horn and A. Paglianti, Gas-liquid Flow and Bubble Size Distribution in Stirred Tanks, *Chemical Engineering Science*, 63 (2008) 2107-2118.
- [11] P. Druault, P. Philippe Guibert and F. Alizon, Use of Proper Orthogonal Decomposition for Time Interpolation from PIV Data: Application to the Cycle-to-cycle Variation Analysis of In-cylinder Engine Flows, *Experiments in Fluids*, 39 (2005) 1009-1023.
- [12] J. Lumley, P. Holmes and G. Berkooz, The Proper Orthogonal Decomposition in the Analysis of Turbulent Flows, *Annual Review of Fluid Mechanics*, 25 (1993) 539-575.
- [13] L. Sirovich, Turbulence and The Dynamics of Coherent Structures PART I : Coherent Structures, *Quarterly of Applied Mathematics*, 45 (1987) 561-571.
- [14] Munson, Young, Okiishi, *Fundamentals of Fluid Mechanics* 3rd ed, Wiley, New York (1998) 612.
- [15] R. Clift, J. R. Grace and M. E. Weber, *Bubbles, Drops and Particles*, Academic press, New York (1978).
- [16] K. C. Kim, Y. U. Min, S. J. Oh, N. H. An, B. Seoudi, H. H. Chun and I. Lee, Time-Resolved PIV Investigation on the Unsteadiness of a Low Reynolds Number Confined Impinging Jet, *Journal of Visualization*, 10 (2007) 367-380.

Seung Jae Yi received his BS degree in Mechanical Engineering from the Pusan National University of Korea (2007) and his MS degree in Mechanical Engineering from the Pusan National University of Korea (2009). He obtained his MS degree with research on bubble-driven flow. His research interests include particle image velocimetry (PIV) measurement technology, characteristics of bio-fluids, and sensing chemistry using MEMS/NANO technology.



Sang Moon Kim is a PhD candidate in the Department of Mechanical Engineering, Pusan National University. He received his Bachelor (1996) and Master (1998) of Engineering degrees from Pusan National University, Department of Mechanical and Production Engineering. His research interests include turbulence measurements, flow visualization, HVAC, and fire simulations.





Hyun Dong Kim is a PhD candidate in the Department of Mechanical Engineering of Pusan National University. He received his MS degree in Mechanical Engineering from Pusan National University in 2005. His main research interest is the development of fluid measurement techniques in the micro-

scale such as micro-PIV, micro-LIF, and defocusing digital PTV. He is also interested in particle manipulation in a micro-channel using a pneumatic micro-pump.



Jong Wook Kim received his BS (Eng) in Mechanical Engineering from the Korea Advanced Institute of Science and Technology (KAIST), Korea, in 1998 and his MS degree in Mechanical Engineering from Hanyang University of Korea in 2000. His research interests include the measurement of thermal

properties of thin film in nano scale using three-omega method and thermal reflectance and characteristics of flow by using proper orthogonal decomposition (POD).



Kyung Chun Kim is a Professor in the School of Mechanical Engineering of Pusan National University in Korea. He obtained his PhD degree from the Korea Advanced Institute of Science and Technology (KAIST), Korea, in 1987. He was selected as a Member of the National Academy of Engineering of

Korea in 2004. His research interests include 3D3C micro-PIV, bio-MEMS, turbulent flow measurements based on PIV/LIF, biomedical engineering, POCT development, wind turbines, and fuel cells.